3406 *Macromolecules* **2005,** *38,* 3406−3413

Stability−Instability Transition by Tuning the Effective Interface Potential in Polymeric Bilayer Films

P. Müller-Buschbaum,*,† O. Wunnicke,‡ M. Stamm,‡ Y.-C. Lin,§ and M. Müller⊥

Physik-Department, LS E13, TU München, James-Franck-Str. 1, 85747 Garching, Germany; Leibniz Inst. für Polymerforschung Dresden, Hohe Str. 6, 01069 Dresden, Germany; Inst. für Physik, WA331, Johannes Gutenberg-Universität, 55099 Mainz, Germany; and Department of Physics, University of Wisconsin−Madison, 1150 University Avenue, Madison, Wisconsin 53706-1390

Received November 19, 2004; Revised Manuscript Received February 1, 2005

ABSTRACT: The wetting behavior of a liquid polymer on top of a supported glassy polymer film is investigated with real (optical microscopy, phase measuring interference microscopy, and scanning force microscopy) and reciprocal space analysis techniques (X-ray reflectivity and grazing incidence small-angle X-ray scattering). The thermodynamic stability of the top film is determined by the interface potential that results from an interplay between short-range and long-range van der Waals contributions. It comprises two competing minima which correspond to a film of vanishingly small, microscopic thickness and to a film with a larger, mesoscopical thickness of a few nanometers. At high temperatures, the liquid top-layer forms drops sitting on top of this mesoscopically thin film. The short-range contribution influences the equilibrium state, and the long-range part of the interface potential determines the kinetics of dewetting. By varying the thickness of the glassy, polymeric sublayer, the effective interface potential is tuned, and a dewetting of the top layer is observed. Additionally, we find the kinetics of hole growth to be compatible with a reduction of the PA sublayer viscosity compared to the bulk.

1. Introduction

Thin polymer films have attracted abiding interest in technical applications and in scientific research. Recently, optical lithography applied to thin films has been utilized in semiconductor industry (thin film imaging). For this special application polymer bilayers, consisting of a thin layer (several 10 nm) on top of a sublayer, are prepared. The wetting behavior of the thin film on top of the sublayer is of crucial importance for the development of polymer structures after light exposure.

In addition to their practical application, polymeric liquids are also promising candidates to experimentally study the statistical mechanics of wetting transitions because (i) the vapor pressure is low and evaporation effects are negligibly small and (ii) polymers do not crystallize easily and the wetting transition is not preemptied by a crystalline phase.

The location of the wetting transition depends on the nature and strength of interactions between the polymer and the substrate.[1,2] Investigating the equilibrium wetting behavior and the kinetics of dewetting,[3] one can extract of a wealth of information about the surface interactions. These surface interactions enter the theoretical description via the effective interface potential $g(h)$ which describes the free energy per area of the liquid film of thickness h on top of a substrate. It is normalized such that $g(h) \to 0$ for $h \to \infty$. Minima of the interface potential correspond to (meta)stable film thicknesses (at conditions where liquid and vapor coexist in the bulk). The contact angle Θ of a drop is related to the depth of the minima via $g(h_{\min}) = \gamma(\cos \Theta - 1)$, where γ is the surface tension of the liquid.

The local curvature of the interface potential determines the kinetics of dewetting. As in bulk thermodynamics, if the second derivative $g''(h)$ is positive, the film will be locally (meta)stable and will dewet (if at all) via nucleation. If the nucleation barrier is low, one might observe homogeneous nucleation by thermal fluctuations. If the nucleation barrier is large, the decay of the metastable film will proceed via heterogeneous nucleation at impurities. If the interface potential exhibits a negative curvature, spinodal dewetting occurs, and the characteristic wavelength and the knowledge of γ allows to quantify $g''(h)$.[4] This strategy has been exploited by Seemann et al.[5] to extract the long-range, van der Waals contribution of the interface potential of polystyrene (PS) on a silicon waver covered with an oxide layer and thereby accurately determine the Hamaker constants.

In general, the interface potential comprises two contributions.[3,43] The long-range contributions stems from the difference between the van der Waals interaction in the fluid and the substrate, $g_{\mathrm{lr}}(h) \sim A/(12\pi h^2)$, where A denotes the Hamaker constant. These long-range forces determine the kinetics of dewetting for film thicknesses larger than a few nanometers. The short-range contribution results from a distortion of the liquid−vapor interface due to the presence of the substrate. To leading order,[6] this interaction decays exponentially fast, $g_{\mathrm{sr}}(l) \sim \gamma \exp(-l/\xi)$. The characteristic length scale is set by the correlation length of density fluctuations, ξ, or the width of the liquid−vapor interface, and the characteristic strength is set by the liquid−vapor tension, γ. In a dense melt, ξ is a microscopic length on the order of a few angstroms.

Using generic values for the Hamaker constant, the interface tension, and the correlation length of density fluctuations, $A \approx 10^{-20}$ J, $\gamma \approx 3 \times 10^{-21}$ J/Å, and $\xi \approx 2$ Å, respectively, one estimates that short-range forces dominate the behavior for extremely thin film thicknesses, $l < \xi \ln(12\pi\gamma\xi^2/A) \approx 8$ Å. Generally, short-range

---

* Corresponding author.

† TU München.

‡ Leibniz Inst. für Polymerforschung Dresden.

§ Johannes Gutenberg-Universität.

⊥ University of Wisconsin−Madison.

10.1021/ma047602d CCC: $30.25

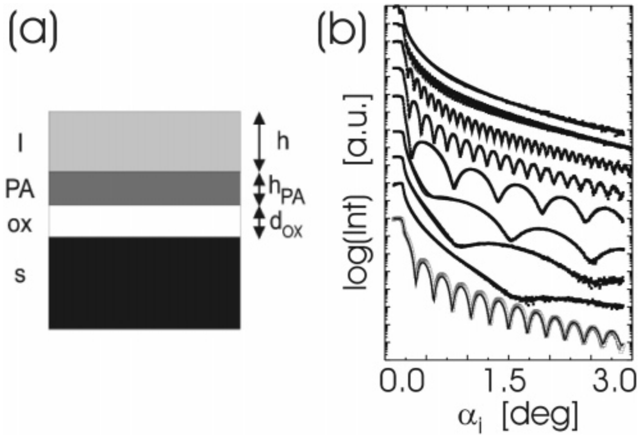

Figure 1. (a) Sketch of the bilayer samples under investigation. (b) X-ray reflectivity data of the single PA layers (filled symbols) before preparation of the PS top layer and of the single PS film (open symbols). The solid lines are fits. The data are shifted for clarity along the intensity axis. From the bottom to the top the thickness increases: only PS, only PA with thickness 1.6, 2.6, 4.4, 8.1, 27.0, 48.7, 128.9, and 600.0 nm.

forces are important because they determine the microscopic film thickness in the dewetted state and influence the contact angle of droplets, and the very same distortion of the interface profile that gives rise to short-range forces leads to the cutoff of the $1/l^2$ divergence of the long-range part.

In our study we investigate a layered substrate where the different layers have Hamaker constants of different signs. In this case the effective Hamaker constant becomes distance-dependent[7] and small due to cancellation effects. Thus, short-range forces become important for somewhat larger film thicknesses. For our system we find that short-range forces modify the interface potential for film thicknesses smaller than 2 nm. Moreover, the interplay between short-range and long-range forces gives rise to a (meta)stable film thickness of the order 1.5 nm,[8] in agreement with the experimental observation of droplets on mesoscopically thin polymer film on oxide-covered substrates.[5,9]

In this work it is demonstrated that the thermodynamic stability (e.g., contact angle) and the dewetting kinetics of a liquid polymer film can efficiently be tuned by introducing a glassy polymer layer between the oxide-covered silicon substrate and the liquid PS. A wetting transition as a function of the sublayer thickness is observed. The mechanism by which the sublayer coating controls wettability is rather general, and the effect might be pertinent to a variety of layered systems.

In the past, several polymeric bilayer systems were investigated, such as brominated PS on PS,[10] PS on poly(dimethylsiloxane) (PDMS),[11] poly(2-vinylpyridine) (PVP) on PS,[12] and polycarbonate (PC) on styrene-*co*-acrylonitrile (SAN).[13,14] A frequently used model system for the investigation of dewetting phenomena in polymeric bilayer films is poly(methyl methacrylate) (PMMA) on PS[15−17] or the reverted system PS on PMMA[18−25] on top of a silicon (Si) surface. The system PS on polyamide-6,I (PA)[26−28] on top of Si (as sketched in Figure 1a) turns out to be particular advantageous because both layers PA and PS are easily prepared by sequential spin-coating. This technique yields top and sublayers of high quality with respect to homogeneity and absence of defects, while other systems require the more complex preparation based on a lift-off process to create the top layer.

A PS film is unstable on top of PA;[26] however, in a bilayer film on top of a coated substrate we observe a stability−instability transition. Via the choice of the thickness of the PA layer, the strength of the destabilizing van der Waals potential and the concomitant time constant of the destabilization process can be tuned.

Our paper is structured as follows: In the following section we describe the sample preparation and the experimental techniques. The subsequent section details our results. In the discussion section we relate the experimental findings to the dependence of the interface potential on the sublayer thickness, and the article closes with a brief summary.

2. Experimental Section

Sample Preparation. Silicon wafers (Si) (100) covered with approximately $d_{ox} \cong 2$ nm of native silicon oxide were used as substrate (Wacker Siltronic, Burghausen, Germany). Prior to spin-coating the substrates were cleaned.[26] The bilayer films (PS on PA) on top of the Si surfaces were prepared by two successive spin-coating steps. The sublayer consists of an amorphous polyamide 6,I (PA) (Bayer AG, Leverkusen, Germany, trademark: Durethan T40) with molecular weight M_w = 28 900 g/mol ($M_w/M_n = 3.28$, $T_g = 130$ °C). A homogeneous polymer layer was obtained by spin-coating out of a PA−1,2-chlorphenol solution (120 s at 1950 rpm). Different sublayer film thicknesses were realized by a concentration series ranging from 0.39 to 117.4 mg/mL. For each sublayer thickness several samples were prepared. The top layer consists of a thin polystyrene (PS) film of low molecular weight (M_w = 1900 g/mol, $M_w/M_n = 1.1$, $T_g = 65$ °C) spin-cast from a PS−toluene solution (30 s at 1950 rpm). All top layers were spin-cast onto the PA sublayer from the same solution, one after the other, to ensure a constant film thickness. The samples were successively annealed on a logarithmic time scale (cyclic, 30 s up to 477 h) in a vacuum furnace and quenched down to room temperature prior to the experimental ex-situ investigations. As a reference, a second set of samples was annealed solely in one step the total annealing time of 477 h. The final states reached within both ways of annealing exhibited identical types of structures observed. At the chosen annealing temperature of $T = 119$ °C the top layer, PS, is liquid. In contrast, bulk PA is solidlike and remains stable during annealing.[26]

Real-Space Techniques. In real space, the sample surface is probed with an increasing in-plane resolution by optical microscopy (OM), phase measuring interference microscopy (PMIM), and scanning force microscopy (SFM). OM images are obtained with magnifications between 4 and 50 times and 2D Fourier transformed to extract dominant lateral length scales on the micrometer range. PMIM data are measured with magnifications of 10 and 100 times at different sample positions. At each, a root-mean-square (rms) surface roughness σ_{rms} is calculated from the height data. SFM data are taken at different scan sizes of 5, 10, and 40 μm using a DI3100 in tapping mode. In addition to the rms roughness, which displays a statistical information perpendicular to the sample surface, a statistical information parallel to the surface is obtained from the power spectral density function (PSD).[29,30] The PSD is calculated from the SFM height data by a 2D Fourier transformation and radial average of the isotropic data in reciprocal space. Because of the different scan ranges in real space, the PSD cover different intervals in the reciprocal space. Thus, a combination of PSD related to different scan ranges enlarges the covered interval in reciprocal space as compared to one individual PSD. All real-space measurements are performed ex-situ, in air at room temperature.

Reciprocal-Space Techniques. In reciprocal space the samples are investigated with X-ray reflectivity (XR) and grazing incidence small-angle X-ray scattering (GISAXS). Ex-situ XR measurements are performed utilizing a laboratory X-ray source (wavelength $\lambda = 0.154$ nm), while in-situ XR

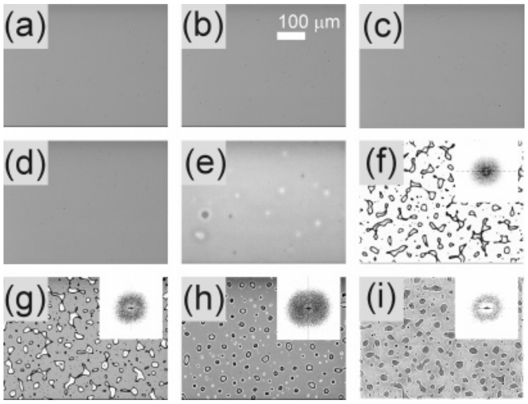

Figure 2. Optical micrographs of the bilayer films after annealing for 477 h at $T = 119$ °C. While the top layer of the samples (a)−(d) remains stable a droplet structure can be observed in the micrographs of the samples (e)−(i). The insets in the micrographs of the samples (f−i) show the 2D Fourier transformation of the images. Abbreviations of the sample types are explained in the text.

measurements become possible with synchrotron radiation at the beamline A2 (DORIS III storage ring at HASYLAB/DESY, Hamburg, $\lambda = 0.15$ nm). From both, the density profile is extracted by fitting the data with a tanh-shaped refractive index profile.[31,32] GISAXS data are recorded at the beamline BW4 (HASYLAB, $\lambda = 0.138$ nm).[33] The beam quality is optimized by using a setup of high-quality entrance cross-slits and a completely evacuated pathway. The scattered intensity is recorded at one fixed incident angle α_i. The chosen incident angle $\alpha_i = 0.534°$ is larger than the critical angles of both polymers as well as of the substrate material which enables an easy separation of the specularly and the diffusely scattered intensity. GISAXS allows for a determination of in-plane structures from a molecular to a mesoscopic regime.[34,35]

3. Results

Figure 1b exhibits the measurement of the PA sublayer film thickness as detected by XR. The PA sublayer films of the different sample types vary in film thickness: (a) 0.0, (b) 1.6, (c) 2.6, (d) 4.4, (e) 8.1, (f) 27.0, (g) 48.7, (h) 128.9, and (i) 600.0 nm. The PS top layers have a fixed film thickness of 19.6 nm within an error of 0.3 nm. This error estimate includes the uncertainty of the fit and deviations between different samples. The abbreviations a−i are used in the following to denote the different sample types. Prior to annealing, a small surface roughness is measured by XR for both the sublayer ($\sigma_{PA} = 0.3$ nm) and the top layer ($\sigma_{PS} = 0.2$ nm) irrespective of the sample type. OM, PMIM, and SFM data additionally confirm the homogeneity of the as-prepared samples.

Figure 2 shows the surface morphology of the samples after 477 h of annealing. The micrographs of the samples with a thick PA sublayer show a dewetted PS top layer (f−i), whereas on a thinner sublayer (a−d) a homogeneous PS surface is observed. Sample (e) shows initial stages of hole formation, but in comparison to the completely dewetted samples (f−i) the destabilization process is retarded. The few dark spots on the homogeneous samples (a−d) are identified by SFM as small contaminations. In comparison to the one-step annealing, a larger number of contaminations accumulate on top of the PS surface during cyclic annealing. However, these contaminations do not cause dewetting via nucleation because, irrespective of the chosen type of annealing (cyclic or one-step), the final states exhibit the same type of surface structure.

Figure 3a presents the temporal evolution of the surface roughness during annealing as detected with PMIM. The samples can be grouped into two classes. Within the first class of samples (a−e) ($h_{PA} = 0{-}8.1$ nm, open symbols in Figure 3a) no change of surface roughness is detected, whereas samples of the second class (f−i) ($h_{PA} = 27.0{-}600.0$ nm, filled symbols in Figure 3a) undergo a significant increase in roughness upon annealing. The early stages are describable by an exponential increase, $\sigma_{PMIM} \propto \exp[t/\tau]$, with a time constant, τ, that depends on the thickness of the sublayer. The inset of Figure 3a depicts the slowing down of the time constant τ with decreasing thickness of the PA sublayer. Thus, we can reduce the destabilizing force on the PS top film by reducing the PA subfilm thickness.

Similar to spinodal decomposition in the bulk, the characteristic length scale of the emerging pattern during spinodal dewetting is expected to decrease upon departing from the limit of metastability by varying the sublayer thickness. No such decrease is observed in Figure 2 because only the final morphology is shown. The final stage provides only very indirect information about the dewetting mechanism.[36] As observable from the time evolution in Figure 3a, the growth of the rms roughness deviates from the expected exponential dependence and becomes significantly slower, suggesting

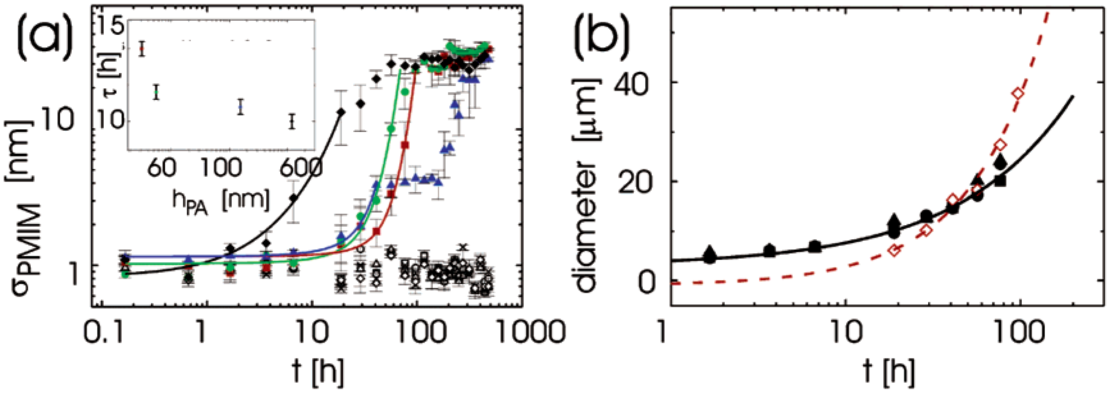

Figure 3. (a) Time dependence of the rms roughness σ_{PMIM} obtained from PMIM measurements (sample type: a, open square; b, open circle; c, open triangle; d, cross; e, open rhomb; f, filled square; g, filled circle; h, filled triangle; i, filled rhomb). The solid lines represent exponential fits $\exp(t/\tau)$. The inset shows the time constant τ as a function of the PA sublayer thickness. (b) Time dependence of the hole diameter obtained from OM measurements (sample type: f, filled squares; g, filled circles; h, filled triangles; i, open rhomb). The solid line represents a fit with exponent $^2/_3$ and the dotted line with exponent 1.

that the late stages shown in Figure 2 are not characteristic of the emerging pattern during spinodal decomposition.

Whereas the surface roughness depicts a statistical information perpendicular to the sample surface, the kinetic of the hole growth yields information about the structure parallel to the surface. For the unstable PA subfilms (h_{PA} = 27.0−600.0 nm), the time-dependent growth of the hole diameter is shown in Figure 3b. If dewetting occurs on a liquid substrate (liquid/liquid dewetting), the substrate viscosity must be taken into account. Then, the dewetting velocity depends on the ratio of the viscosity of the polymer (top layer) η_f and the substrate (sublayer) η_s.[37] For $\eta_f/\theta < \eta_s$ (θ denoting the contact angle in the equilibrium, dewetted state) the hole diameter, d, grows according to $d \sim t$. In the opposite limit, $\eta_f/\theta > \eta_s$; however, the diameter grows like $d \sim t^{2/3}$. The values 1 and $^2/_3$ mark the limiting values of the hole growth exponent for liquid/solid and liquid/liquid dewetting, respectively. The solid and the dotted lines show these two limits in Figure 3b. Within the range of the rather large experimental error, the observed hole growth in the case of PA film thicknesses between 27 and 129 nm apparently agrees better with the prediction for liquid/liquid dewetting. Although the bulk glass transition temperature of PA is well above the annealing temperature and, thus, the condition $\eta_f/\theta < \eta_s$ satisfied for the bulk viscosities, thin PA films apparently behave more liquidlike as judged from the dewetting kinetics of the PS top film. This observation would suggest a decrease of the glass transition temperature of PA upon decreasing the PA film thickness.[38] For larger thicknesses of the PA sublayer, the observed hole growth starts to deviate from the $d \sim t^{2/3}$ behavior, and for PA film thicknesses as large as 600 nm (open symbols in Figure 3b) it follows rather closely the behavior of dewetting on a solid substrate with a growth exponent of 1. The observed change of the time evolution of the hole diameter can be interpreted as a crossover from a more liquid-like to a solid-like behavior of the PA film with increasing thickness.[39]

For a statistical analysis of the OM data the images are 2D Fourier transformed, yielding a ring of intensity in Fourier space (see insets in Figure 2f−i). The corresponding dominant in-plane lengths are calculated from the position of the intensity maxima after a radial average (see position of arrows in Figure 4a). With increasing PA sublayer thickness the peak position slightly shifts toward smaller values of q. From the corresponding length scale in real space we conclude that the Fourier rings are related to the drop diameter. The drop diameter slightly decreases from 13.5 μm (sample f) to 11.5 μm (sample i). This decrease basically reflects mass conservation because the thickness of the destabilized PS layer was identical.

Additionally, a second and significantly smaller nanostructure is detected with SFM (see Figure 5). It is located between the large drops created by the dewetting of the PS layer. In addition, it is observed inside the holes of sample (e) which exhibits a retarded dewetting. Thus, this nanostructure (droplets) coexists with the optically observable dewetting structure (drops). The height of the nanostructure is similar for all samples and largely independent of the PA sublayer thickness (see line scans shown in Figure 5). Again the 2D Fourier transformed data exhibit a well-pronounced ring of intensity in Fourier space. The PSD calculated after radial averaging of the Fourier data are plotted in Figure 4b. The corresponding dominant in-plane length resembles the distance between droplets. Its values increase from 300 nm (sample e) to 450 nm (sample i) with increasing PA layer thickness. The presence of the nanostructure is confirmed with GISAXS measurements detecting an increased intensity at the corresponding position in reciprocal space. Since GISAXS samples a larger surface area as compared to SFM, these data prove the statistical relevance of the nanostructure shown in Figure 5 and rule out artifacts due to possible surface modifications by the SFM tip.

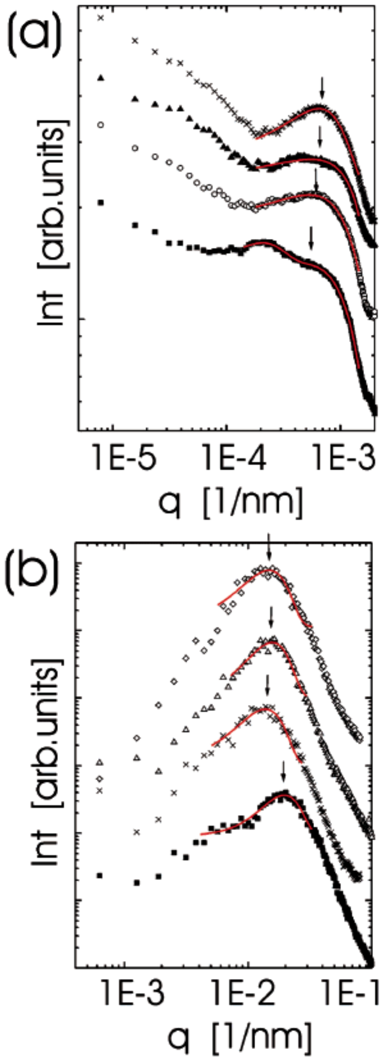

Figure 4. (a) PSD calculated from the OM data and (b) from the SFM height data by a 2D Fourier transformation and radial average of the isotropic Fourier space data. The PA film thickness increases from the bottom to the top: 27.0, 48.7, 128.9, and 600.0 nm. The solid lines are a fit to determine the q-space position of the intensity maximum. The curves are shifted along the intensity axis for clarity.

4. Discussion

To understand the observed kinetics of dewetting, we relate the large-distance behavior of the interface potential at the initial thickness of the PS top layer, $h \equiv h_{PS}$ = 19.6 nm, to the long-range part of the interface potential. To rationalize the occurrence of a second, smaller dewetting structure (and to obtain information about the equilibrium, dewetted state), we also have to consider the short-distance behavior of the interface

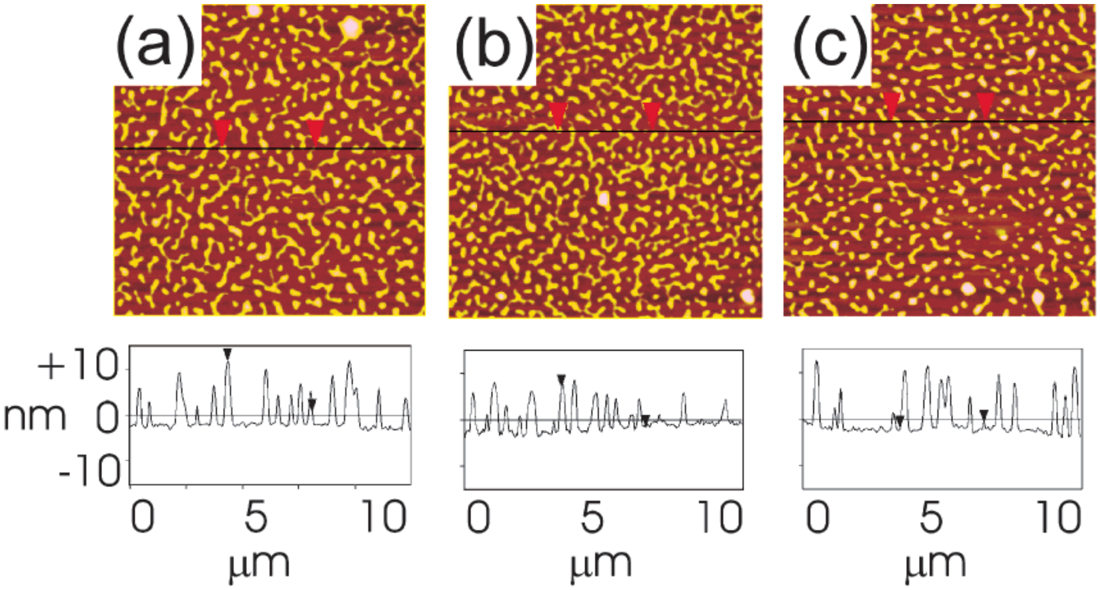

Figure 5. Example of the surface morphology as detected with SFM between the large drops of sample with PA film thickness of (a) 48.7, (b) 128.9, and (c) 600.0 nm. The scan range is 10 × 10 μm^2, and the selected line scan depicts the height of the surface structure.

potential. The latter results from a subtle interplay between short-range and long-range contributions to the interface potential while the former is solely determined by the long-range part. By tuning the thickness of the PA sublayer, we change the long-range contribution to the interface potential and thus affect the interface potential at both short and large distances.

As mentioned in the Introduction, the van der Waals interactions result in a long-range interaction $g_{\mathrm{vdW}}(h)$, $h \equiv h_{\mathrm{PS}}$, and the distortion of the density profile in the vicinity of the substrate gives rise to a short-range contribution $g_{\mathrm{SR}}(h)$. We have previously utilized self-consistent-field theory[8] to calculate the interface potential from a microscopic theory. Within the mean-field approximation we described the detailed shape of the density profile and the molecular conformations. Thus, we calculated the interface potential taking due account of long-range van der Waals interactions and both the distortion of the density profile and the change of the chain conformations in thin films, which gives rise to the short-range contribution, g_{SR}.[40] Those detailed self-consistent-field calculations suggested that the salient qualitative features of the interface potential are well describable by a superposition approximation, $g(h) = g_{\mathrm{SR}}(h) + g_{\mathrm{vdW}}(h)$. In the following we rather utilize phenomenological considerations based upon the simple expressions for the short-range and long-range contribution (see eqs 1 and 2) than detailed self-consistent-field calculations to illustrate the qualitative behavior.

The long-range part stems from the attractive van der Waals interactions in the fluid and between the fluid and the substrate. It can be obtained as a convolution of the interaction potential with the normalized density profile $\phi_h(z)$ of the liquid film of thickness h (measured in units of the density of the liquid that coexists with the vapor).

$$\frac{g_{\mathrm{vdW}}(h)}{\gamma} = -\int \mathrm{d}z\ [\phi_h(z) - \phi_\infty(z)]\frac{1}{6\pi\gamma}\left[\frac{A_{\mathrm{PSPS}} - A_{\mathrm{PSPA}}}{z^3} - \frac{A_{\mathrm{PSox}} - A_{\mathrm{PSPA}}}{(z + h_{\mathrm{PA}})^3} - \frac{A_{\mathrm{PSSi}} - A_{\mathrm{PSox}}}{(z + d_{\mathrm{ox}} + h)^3}\right]$$
$$= \frac{\eta(h)}{12\pi\gamma}\left[-\frac{A_{\mathrm{PSPS}} - A_{\mathrm{PSPA}}}{h^2} + \frac{A_{\mathrm{PSox}} - A_{\mathrm{PSPA}}}{(h + h_{\mathrm{PA}})^2} + \frac{A_{\mathrm{PSSi}} - A_{\mathrm{PSox}}}{(h + d_{\mathrm{ox}} + h_{\mathrm{PA}})^2}\right] \quad (1)$$

The latter equation defines the function $\eta(h)$: If the density profile were a sharp kink, i.e., $\phi_h(z) = 1$ for $0 \le z \le h$ and vanished otherwise, $\eta(h)$ would be unity everywhere. Then, the long-range contribution to the interface potential would diverge as $h \to 0$. This unphysical behavior is an artifact of the sharp kink approximation and upsets the simple superposition $g(h) = g_{\mathrm{SR}}(h) + g_{\mathrm{vdW}}(h)$. Instead, one expects $g_{\mathrm{vdW}}(h) \to$ const for $h \to 0$ because there simply is no PS liquid to experience any van der Waals attraction. In principle, detailed self-consistent-field calculation could provide the density profile and $g(h)$.[8] To illustrate the qualitative effect, here, a plausible Ansatz for the density profile is made

$$\phi_h(z) = \frac{1}{2}\left[1 - \tanh\left(\frac{z - h}{w}\right)\right]\left[1 - \exp\left(-\alpha\left(\frac{z}{w}\right)^4\right)\right] \quad (2)$$

where w characterizes the width of the liquid–vapor interface. The first factor describes the liquid–vapor interface, while the second factor parametrizes the vanishing of the density at the substrate. Of course, this is a very crude approximation of the density profile of PS; for instance, packing effects are completely neglected. Nevertheless, it captures the salient qualitative features at the substrate and the liquid–vapor interface and removes the unphysical divergence of the sharp-kink approximation for $h \to 0$. The density profile and the function η are shown as insets of Figure 6. For large thicknesses, $h \gg w$, the result of the sharp kink approximation, i.e., $\eta(h) = 1 + \mathcal{O}[(w/h)^2]$ is recovered. The combination of Hamaker constants[41] $(A_{\mathrm{PSSI}} - A_{\mathrm{PSox}})/(A_{\mathrm{PSPS}} - A_{\mathrm{PSox}}) = 6.9$ is chosen, in accordance with the experiments of Seemann et al.[5] and our previous calculations.[8]

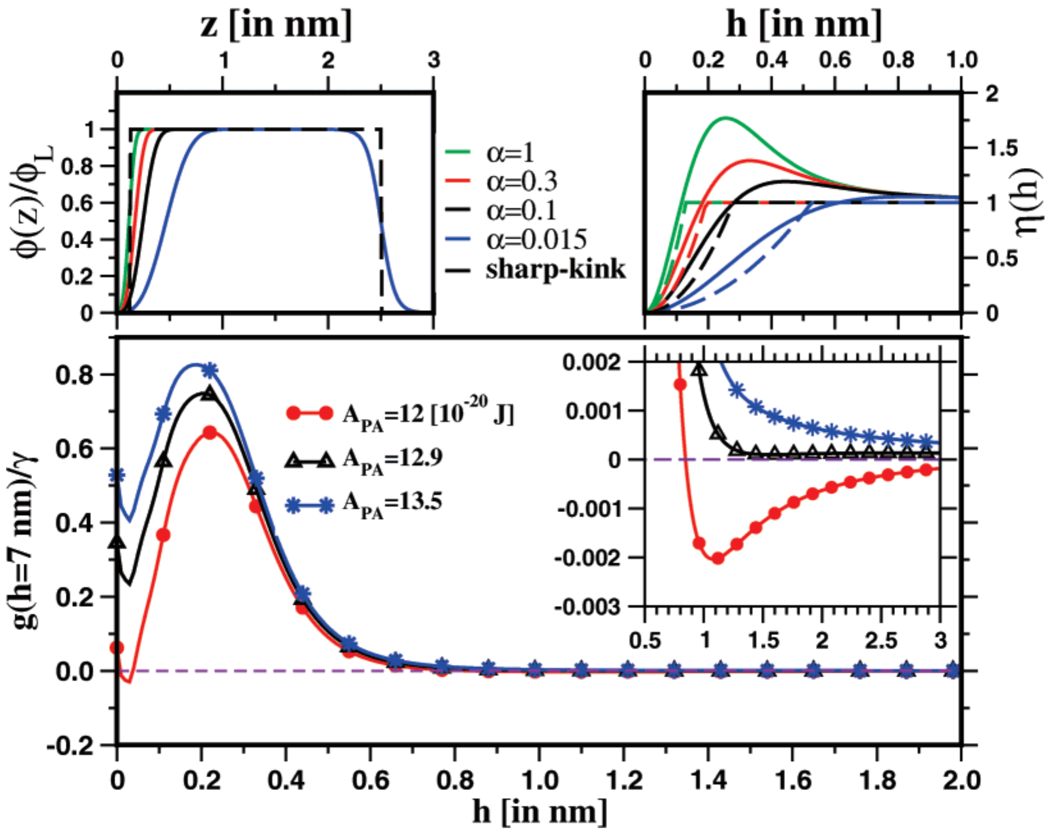

Figure 6. Top: density profiles (left) described by eq 2 and the function $\eta(h)$ (right) defined in eq 1. The dashed lines correspond to the sharp-kink approximation for varying gap widths (cf. left panel) between the liquid (PS) and the substrate (PA). Bottom: $g(h)/\gamma$ for various values of the Hamaker constant A_{PA} and fixed $h_{\mathrm{PA}} = 7$ nm. The inset shows an enlarged view of the minimum at the mesoscopic film thickness.

The short-range contribution takes the form

$$\frac{g_{\mathrm{SR}}(h)}{\gamma} = \sum_{k=1} a_k \exp\left(-k\,\frac{h}{w}\right) \qquad (3)$$

where a_i are constants of order unity and w the length scale with which the liquid−vapor interface profile approaches the bulk density. For the present phenomenological considerations we have obtained the coefficients a_i by fitting our self-consistent-field results for a PS film.[8]

The superposition of the two contributions results in an interface potential with two minima: One is a vanishingly small PS film thickness, $h \approx 0$, and originates exclusively from the short-range interactions. It mirrors the free energy cost to build a liquid layer of the thickness of the interfacial width. Whether or not this minimum is thermodynamically stable depends on the very details of the interactions between the fluid and the substrate. Its free energy is difficult to predict because the interactions on the atomistic scale (per segment) are orders of magnitude larger ($\mathcal{O}$(eV)) than the typical value of the interface potential ($\mathcal{O}$(meV/Å^2)). Therefore, it is very sensitive to the surface preparation. In view of the difference in free energy scale it is impossible to relate these fine details of the interface potential to a specific type of surface interaction or the cleaning protocol. The second minimum at a mesoscopical thickness of a few nanometers results from a competition between the rapidly decaying repulsion of the short-range forces and the weak attraction due to the van der Waals contribution. Unlike the first minimum, the stability of the minimum at a larger, mesoscopical thickness can be tuned by the thickness of the sublayer (here PA).

In the following, we utilize this simple phenomenological scheme to qualitatively rationalize the experimentally observed wetting behavior. While for liquid substrates, there are several possibilities to tune the long-range forces, for example, by changing the pressure or adding salt to the liquid substrate,[44] choosing the thickness of a glassy sublayer is a convenient mechanism to control the wettability of solid substrates.

In Figure 6, the interface potentials are shown as a function of A_{PA} at sublayer thickness $h_{\mathrm{PA}} = 7$ nm. For $A_{\mathrm{PA}} = 12.8 \times 10^{-20}$ J a first-order wetting transition results. This value is compatible with alternative estimates of the Hamaker constant.[42] In Figure 7 this value of A_{PA} is utilized to calculate the interface potential for different thicknesses of the PS top layer, h_{PA}.

The equilibrium wetting properties are related to the minimum at mesoscopic film thickness, and its stability sensitively depends on the thickness of the PA sublayer and temperature. Our phenomenological calculations in Figure 7 suggest that after the dewetting at high temperature there remains a stable, mesoscopically thick film for large sublayer thicknesses, h_{PA}. The thickness of this remaining PS film is suggested to be on the order $h \approx 1.5$ nm.

In the melt state at high temperature, in-situ XR measurements show the dewetting of the PS liquid into a morphology of macroscopic drops via a strong damping of the Kiessing oscillations and, indeed, reveal the existence of a homogeneous mesoscopic layer on top of the PA sublayer. Thus, at high temperature there are macroscopic drops sitting on top of a mesoscopically

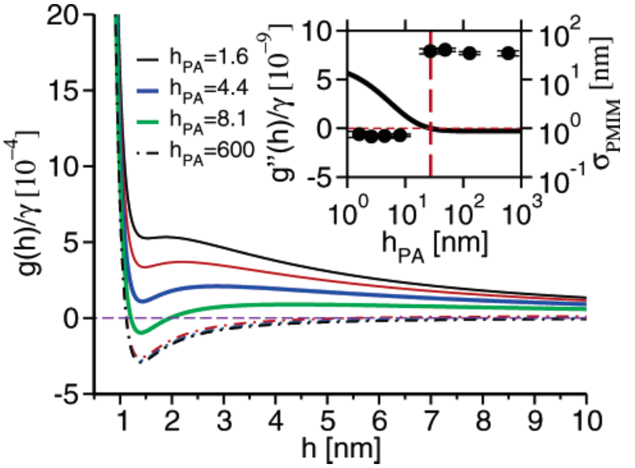

Figure 7. $g(h)$ for various h_{PA}. The Hamaker constant $A_{PA} = 12.8 \times 10^{-20}$ J is estimated by the experimental results showing that the PS film dewets on top of a PA sublayer above the thickness of $h_{PA} = 8.1$ nm. The inset shows the curvature of the effective interface potential, $g''(h)$ (solid line), for PS film thickness $h = 19.6$ nm as a function of the PA sublayer thickness. The vertical dashed line located at $h_{PA} = 27.5$ nm indicates the boundary between spinodal dewetting ($g''(h) < 0$) and nucleation ($g''(h) > 0$). The filled circles are PMIM measured surface roughness in the final annealing state.

thick film. The experimental thickness of the mesoscopically thin layer, e.g., $h_{min} = 4.3 \pm 1$ nm for sample (g), is somewhat larger than in the phenomenological considerations. We emphasize, however, that our phenomenological calculations do not incorporate any information about the local interactions between PA and PS at the interface between the sublayer and the top layer but rather utilize a parametrization of the short-range contribution for a PS oxide interface. In view of the rather delicate dependence of the short-distance behavior of the interface potential on the microscopic structure (interactions between PS and PA on the atomistic scale, roughness of the interface), we consider this order of magnitude agreement satisfactorily.

Upon quenching the sample to room temperature, we destabilize the mesoscopically thick layer that formed a stable, laterally homogeneous layer at high temperature, and this second dewetting process gives rise to the formation of the smaller-scale dewetting structure—the droplets between the macroscopically large drops. As the sample is quenched to room temperature, the mesoscopically layer not only dewets, but the PS top layer additionally vitrifies. Therefore, droplets on a significantly smaller scale form by dewetting of a film of nanometer thickness, but those droplets do not coalesce. As a result, a dewetting morphology with two distinct length scales becomes experimentally observable: the optically visible dewetting structure (see Figure 2) and the nanostructure observable by SFM (see Figure 5). A similar behavior has been observed in the system PS on Si depending on the thickness of the oxide layer.[8,9]

While the equilibrium states depend on the minima of the interface potential, the kinetic behavior for thick PS layers depends only on the long-range van der Waals contribution.[5] In the inset, the curvature of the interface potential is shown for $h = 19.6$ nm as a function of the sublayer thickness h_{PA}. It provides a consistent description of the experimentally observed kinetics (cf. Figure 3a). For small h_{PA} the curvature of $g(h)$ is positive, leading to dewetting via nucleation, while for large PA sublayer thicknesses the curvature becomes negative and we observe spinodal-like dewetting in the experiment.

5. Summary

In summary, we have investigated the dewetting morphology of a bilayer system, consisting of liquid PS on top of a glassy PA film supported by a silicon substrate by real- and reciprocal-space techniques.

The interface potential of the layered substrate comprises two competing minima: the minimum at $h \approx 0$ originates from the short-range interactions, while the minimum at mesoscopical thickness results from an interplay between short- and long-range interactions. The presence of two minima in the interface potential gives rise to a two-step dewetting process upon quenching to room temperature that results in a large-scale dewetting structure (drops) and a smaller nanostructure, which is present inside the dewetted areas. It is important to note that both are present all over a large sample surface range of several centimeters as probed with optical and scattering techniques.

This interplay enables an easy control of the wettability of the PA-coated substrate by tuning the thickness of the PA sublayer. Only in the case of thick PA sublayers is dewetting experimentally observed, and it occurs faster the thicker the PA sublayer is. The phenomenological calculations suggest that both the free energy of the minimum of the interface potential at mesoscopical thickness decreases as well as the curvature of the interface potential at large PS film thickness changes sign as we increase the thickness of the PA sublayer. The former effect is related to the short-distance behavior of $g(h)$, and it causes an equilibrium wetting transition and a concomitant increase of the contact angle upon increasing h_{PA}. The latter effects reveals the large-distance behavior of the $g(h)$ and suggests that the kinetics of dewetting changes from nucleation to spinodal dewetting upon increasing h_{PA}. Within the chosen parameter range of the PA and PS film thickness the destabilizing van der Waals potential is so weak, that this wetting transition becomes conveniently observable with ex-situ experimental techniques. The observed kinetics of the hole growth additionally suggests that the PA layer becomes less glassy with decreasing thickness than expected for bulk PA.

Because the mechanism by which the sublayer coating controls wettability is rather general, we expect the reported effect will be observable in a variety of other layered systems and might be useful for controlling the wettability.

Acknowledgment. We thank A. Meyer and R. Döhrmann (A2) and S. Cunis (BW4) for their help during setting up the synchrotron beamlines at the HASYLAB and R. Gehrke for his general support. C. Lorenz-Haas and C. Casignol helped during the synchrotron experiments and S. Kummer with the ex-situ X-ray measurements. We thank K. Binder for stimulating discussions. The used silicon substrates were kindly provided by Wacker Siltronic, Burghausen (Germany). This work was supported by the DFG priority program "Benetzung und Strukturbildung an Grenzflächen" under Grants Sta324/8 and Bi314/17.

References and Notes

(1) Dietrich, S. *Phase Transitions and Critical Phenomena*; Academic: New York, 1988; Vol. 12.

(2) Binder, K.; Landau, D. P.; Müller, M. *J. Stat. Phys.* **2003**, *110*, 1411.

(3) de Gennes, P. G. *Rev. Mod. Phys.* **1985**, *57*, 827.

(4) Vrij, A.; Overbeek, J. T. G. *J. Am. Chem. Soc.* **1968**, *90*, 3074.

(5) Seemann, R.; Herminghaus, S.; Jacobs, K. *Phys. Rev. Lett.* **2001**, *86*, 5534; *J. Phys.: Condens. Matter* **2001**, *13*, 4915.

(6) Chain end effects give rise to interactions on the length scale of a whole molecule [see: Semenov, A. N. *J. Phys. II* **1996**, *6*, 1757)]. They are automatically captured by the self-consistent-field calculations of ref 8, but they are neglected in the following phenomenological calculations.

(7) Cazabat, A. M. In *Les Houches*, *Liquids at Interfaces*; Charvolin, J., Joanny, J. F., Zinn-Justin, J., Eds.; Elsevier Science Publishers: Amsterdam, 1990; p 374.

(8) Müller, M.; MacDowell, L. G.; Müller-Buschbaum, P.; Wunnicke, O.; Stamm, M. *J. Chem. Phys.* **2001**, *115*, 9960.

(9) Müller-Buschbaum, P.; Vanhoorne, P.; Scheumann, V.; Stamm, M. *Europhys. Lett.* **1997**, *40*, 655.

(10) Ade, H.; Winesett, D. A.; Smith, A. P.; Andres, S.; Stammler, T.; Heske, C.; Slep, D.; Rafailovich, M. H.; Sokolov, J.; Stöhr, J. *Appl. Phys. Lett.* **1998**, *73*, 3775.

(11) David, M. O.; Reiter, G.; Sitthai, T.; Schultz, J. *Langmuir* **1998**, *14*, 5667.

(12) Kang, H.; Lee, S. H.; Kim, S.; Char, K. *Macromolecules* **2003**, *36*, 8579.

(13) Faldi, A.; Composto, R. J.; Winey, K. I. *Langmuir* **1995**, *11*, 4855.

(14) Pan, Q.; Winey, K. I.; Hu, H. H.; Composto, R. J. *Langmuir* **1997**, *13*, 1758.

(15) Sferrazza, M.; Heppenstall-Butler, M.; Cubitt, R.; Bucknall, D.; Webster, J.; Jones, R. A. L. *Phys. Rev. Lett.* **1998**, *81*, 5173.

(16) Higgins, A. M.; Jones, R. A. L. *Nature (London)* **2000**, *404*, 476.

(17) Higgins, A. M.; Sferrazza, M.; Jones, R. A. L.; Jukes, P. C.; Sharp, J. S.; Dryden, L. E.; Webster, J. *Eur. Phys. J. E* **2002**, *8*, 137.

(18) Harris, M.; Appel, G.; Ade, H. *Macromolecules* **2003**, *36*, 3307.

(19) Krausch, G. *J. Phys.: Condens. Matter* **1997**, *9*, 7741.

(20) Lambooy, P.; Phelan, K. C.; Haugg, O.; Krausch, G. *Phys. Rev. Lett.* **1996**, *76*, 1110.

(21) Lin, Z.; Kerle, T.; Russell, T. P.; Schaffer, E.; Steiner, U. *Macromolecules* **2002**, *35*, 6255.

(22) Qu, S.; Clarke, C. J.; Liu, Y.; Rafailovich, M. H.; Sokolov, J.; Phelan, K. C.; Krausch, G. *Macromolecules* **1997**, *30*, 3640.

(23) Wang, C.; Krausch, G.; Geoghegan, M. *Langmuir* **2001**, *17*, 6269.

(24) Wei, B.; Genzer, J.; Spontak, R. J. *Langmuir* **2004**, *20*, 8659.

(25) Yuan, C.; Ouyang, M.; Koberstein, J. T. *Macromolecules* **1999**, *32*, 2329.

(26) Renger, C.; Müller-Buschbaum, P.; Stamm, M.; Hinrichsen, G. *Macromolecules* **2000**, *33*, 8388.

(27) Wunnicke, O.; Lorenz-Haas, C.; Müller-Buschbaum, P.; Leiner, V.; Stamm, M. *Appl. Phys. A* **2002**, *74*, S445.

(28) Wunnicke, O.; Müller-Buschbaum, P.; Wolkenhauer, M.; Lorenz-Haas, C.; Cubitt, R.; Leiner, V.; Stamm, M. *Langmuir* **2003**, *19*, 8511.

(29) Gutmann, J. S.; Müller-Buschbaum, P.; Stamm, M. *Faraday Discuss.* **1999**, *112*, 285.

(30) Müller-Buschbaum, P.; Gutmann, J. S.; Stamm, M. *Macromolecules* **2000**, *33*, 4886.

(31) Parrat, L. G. *Phys. Rev.* **1954**, *55*, 359.

(32) Lekner, J. *Theory of Reflection*; Martinus Nijhoff Publishers: Dordrecht, 1987.

(33) Gehrke, R. *Rev. Sci. Instrum.* **1992**, *63*, 455.

(34) Naudon, A.; Babonneau, D.; Thiaudiere, D.; Lequien, S. *Physica B* **2000**, *283*, 69.

(35) Müller-Buschbaum, P. *Anal. Bioanal. Chem.* **2003**, *376*, 3.

(36) Herminghaus, S.; Jacobs, K.; Mecke, K.; Bischof, J.; Fery, A.; Ibn-Elhaj, M.; Schlagowski, S. *Science* **1998**, *282*, 916.

(37) Brochard-Wyart, F.; Martin, P.; Redon, C. *Langmuir* **1993**, *9*, 3682.

(38) Hartmann, L.; Gorbatschow, W.; Hauwede, J.; Kremer, F. *Eur. Phys. J. E* **2002**, *8*, 145.

(39) Forrest, J. A. *Eur. Phys. J. E* **2002**, *8*, 261.

(40) Beyond the mean-field approximation several effects modify the interface potential: (i) Capillary waves lead to a renormalization of the interface potential [Lipowsky, R.; Fischer, M. E. *Phys. Rev. B* **1987**, *36*, 2126]. (ii) Excluded-volume effects give rise to long-range correlations on the length scale between the width of the liquid−vapor interface and the chain extension in the bulk [Müller, M.; Binder, K.; Schäfer, L. *Macromolecules* **2000**, *33*, 4568; Wittmer, J. P., et al. *Phys. Rev. Lett.* **2004**, *93*, 147801] and thin films [Müller, M. *J. Chem. Phys.* **2002**, *116*, 9930; Cavallo, A., et al. *J. Phys.: Condens. Matter*, in press]. Both types of fluctuation effects are neglected in the following.

(41) Visser, J. *Adv. Colloid Interface Sci.* **1972**, *3*, 331.

(42) Hermsdorf, N.; Wunnicke, O.; Müller-Buschbaum, P., to be published.

(43) Schick, M. In *Les Houches Lectures on Liquids at Interfaces*; Charvolin, J., Joanny, J. F., Zinn-Justin, J., Eds.; Elsevier Science Publishers B.V.: Amsterdam, 1990.

(44) Bonn, D.; Bertrand, E.; Meunier, J.; Blossey, R. *Phys. Rev. Lett.* **2000**, *84*, 4661.

MA047602D